Journal of MATERIALS RESEARCH

Article
DOI:10.1557/s43578-022-00681-4

Crack length estimations for small-scale fracture experiments via image processing techniques

K. Schmuck[1,a], M. Alfreider[1], D. Kiener[1]

[1] Department of Materials Science, Chair of Materials Physics, Montanuniversität Leoben, Jahnstraße 12, Leoben, Austria
[a] Address all correspondence to this author. e-mail: klemens.schmuck@unileoben.ac.at

Received: 22 November 2021; accepted: 26 July 2022; published online: 31 August 2022

Accurate knowledge of the current crack length is crucial to evaluate fracture mechanical tests. At the sub-micron to micron scale, the crack length is directly accessible via observation during in-situ experiments in electron microscopes, or indirectly via calculation from sample stiffness. In the current work, image processing techniques were used to introduce a semi-automatic technique to measure crack lengths at the micron scale from image sequences. The technique utilizes manually defined filters and searches for contours near the previous crack tip locating the new one according to the previous position. To demonstrate validity and capability, three micron-sized notched cantilevers were prepared for bending experiments and tested in-situ by partial unloading. Comparison of crack lengths determined by the proposed method, manual measurement and sample stiffness revealed a reasonable agreement, while occasional deviations allow further insights into the crack behaviour. Thus, our new approach enables more in-depth investigation of small-scale fracture processes.

Introduction

To study material behaviour at ever decreasing dimensions, small scale experiments are frequently conducted, allowing to test not only confined volumes [1–3], but also individual layers of multilayer stacks [4], hard coatings [5], individual grain boundaries [6] and/or specific interfaces [7]. Due to ongoing device miniaturization and shrinking internal length scales [8, 9], these miniaturized approaches were also extended to fracture experiments at the micron to submicron scale. Furthermore, performing such experiments in situ allows additional insights into both fracture processes and material behaviour on small length scales [10, 11].

However, the fracture mechanical evaluation relies on accurate knowledge of the crack characteristics, especially the crack length. On the macroscopic scale crack length is measured via optical observations or well-established methods such as the potential drop method [12], the partial unloading technique [13] or digital image correlation (DIC) [14]. The potential drop method is hardly applicable at the micron to sub-micron scale due to small sample dimensions. Classical DIC requires native or artificial patterns on the sample surface to track deformation or shape changes. Hence, DIC is not straight forward applicable to ion beam polished surfaces and therefore, the crack length is typically evaluated manually from captured images, which is a tedious task. Partial unloading allows the crack length to be estimated at the unloading steps by measuring sample stiffness changes [15]. Inspired by the crack length measurement via partial unloading, Ast et al. [16] developed a method to estimate the crack length based on a continuous stiffness signal, which is obtained by superimposing a small harmonic displacement signal over the constant displacement rate. By utilizing finite element analysis or analytical methods, sample stiffness can be converted into a crack length assuming a straight crack front [17–20].

However, it is not always possible to measure the continuous stiffness signal, e.g. in older systems or for very ductile materials which only exhibit blunting. In such cases the crack length is most often estimated manually. As this is time-consuming and dependent on human individuality, the current work proposes a new semi-automatic approach utilizing image processing techniques. We discuss the application of the image processing technique in more detail, and the derived data are compared with results from cantilever stiffness calculations and manual evaluations. Three in-situ sub-micron bending tests were performed with different specimen sizes made from a nanocrystalline W-Cu 20 wt% composite as a model isotropic material.

© The Author(s) 2022

This semi-brittle material represents a challenging test case to highlight the general applicability of our concept to a wide range of problems.

Results

The crack lengths determined by the developed algorithm were compared to manually measured crack lengths and those calculated from unloading stiffness at the individual unloading steps. The manual measurements of the crack length was taken first to avoid biased evaluation. This was performed independently several times from the top cantilever surface to the assumed crack tip. The final manual measured crack length is the mean of all measured lengths taken from one frame, while the minimal and maximal manually measured values are expressed by the error bars in Figs. 1(a), 2(a) and 3(a), respectively. The gathered raw load–displacement curves are given for each sample in the supplementary.

Figure 1(a) displays the crack lengths determined in the largest cantilever ($34.3 \times 31.8\ \mu m^2$) up to a maximum displacement of 32 µm. In general, the different methods to determine the crack length agree well. There are some minor differences, which will be detailed in the following to give better insight into the different methodologies. The micrograph in Fig. 1(b) depicts the crack on the sample surface at the first unloading step, which was purely elastic. Among the unloading steps from position b to c, the determined crack lengths of all three techniques agree well. Clearly, starting at position c in Fig. 1(a) the crack length determined from unloading stiffness deviates from the crack length measured in the images. This might stem from crack growth inside the sample, which is not visible on any sample surface. But also from the faint crack growth in front of the algorithmically determined crack, which is an inconspicuous feature compared to the fabrication curtain of the focused ion beam (FIB) (Fig. 1(d, e)). The deviation of about 2.2 µm between the mechanical and image-based methods remained roughly constant until the last unloading step. Algorithmically and manually measured crack lengths agree well. Small deviations arise from material bridging, tearing and elastic crack closure due to partial unloading. These effects make manual crack evaluation rather challenging. Detailed inspection of intermediate loading frames showed that the formed material bridges were cracked already, which was not discernable from the frames used for manual measurement.

Results obtained for the medium-sized cantilever ($14.2 \times 13.8\ \mu m^2$) are shown in Fig. 2(a). The sample surface at the first unloading step is depicted in Fig. 2(b). At the beginning, the crack length calculated from the unloading stiffness revealed a non-physical crack length reduction of about 500 nm and 300 nm for the second and third unloading steps, respectively.

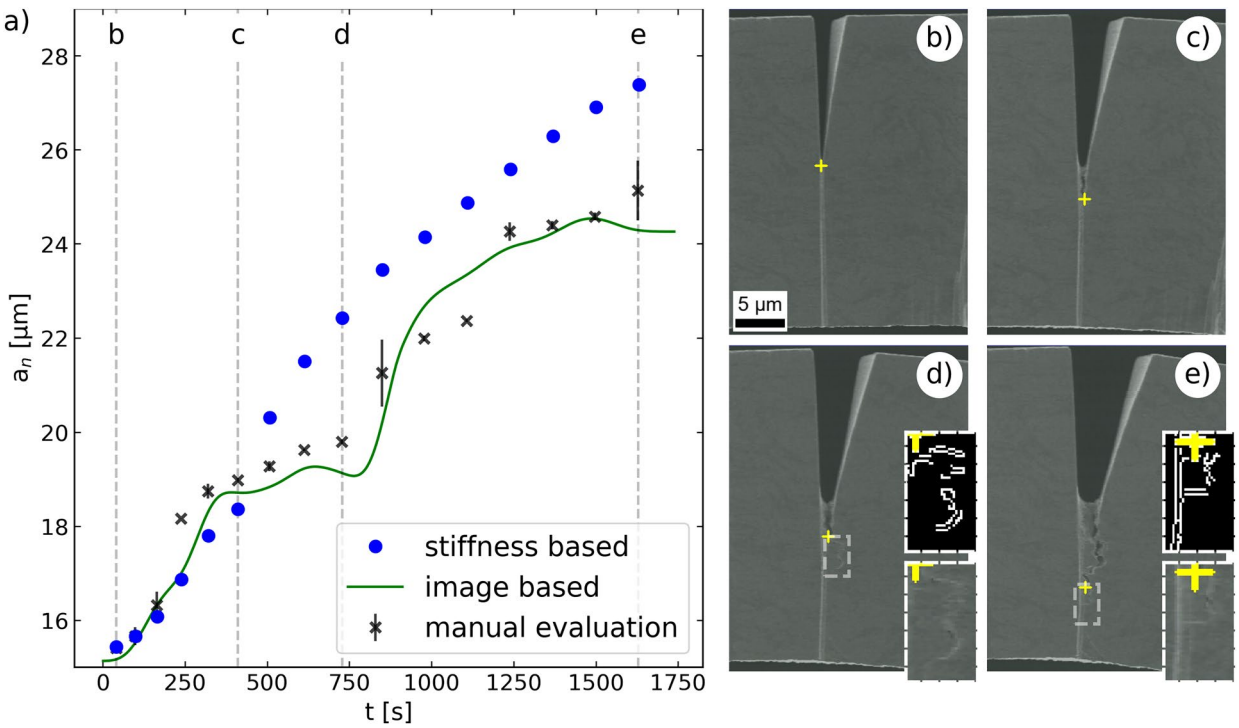

Figure 1: (a) Determined crack lengths a_n for the largest cantilever with a cross-section of $34.3 \times 31.4\ \mu m^2$. At each unloading step the crack length was manually measured (black crosses) and calculated from unloading stiffness (blue dots), while the algorithm also determined the crack lengths of all images (solid green line). (b–e) Micrographs of the cracked sample surface at different unloading steps indicated by vertical dashed gray lines in (a). The crack tip is marked with a yellow cross, whereas the zoomed insets in (c) and (d) show a thin crack in front of the algorithmically identified crack tip.

© The Author(s) 2022

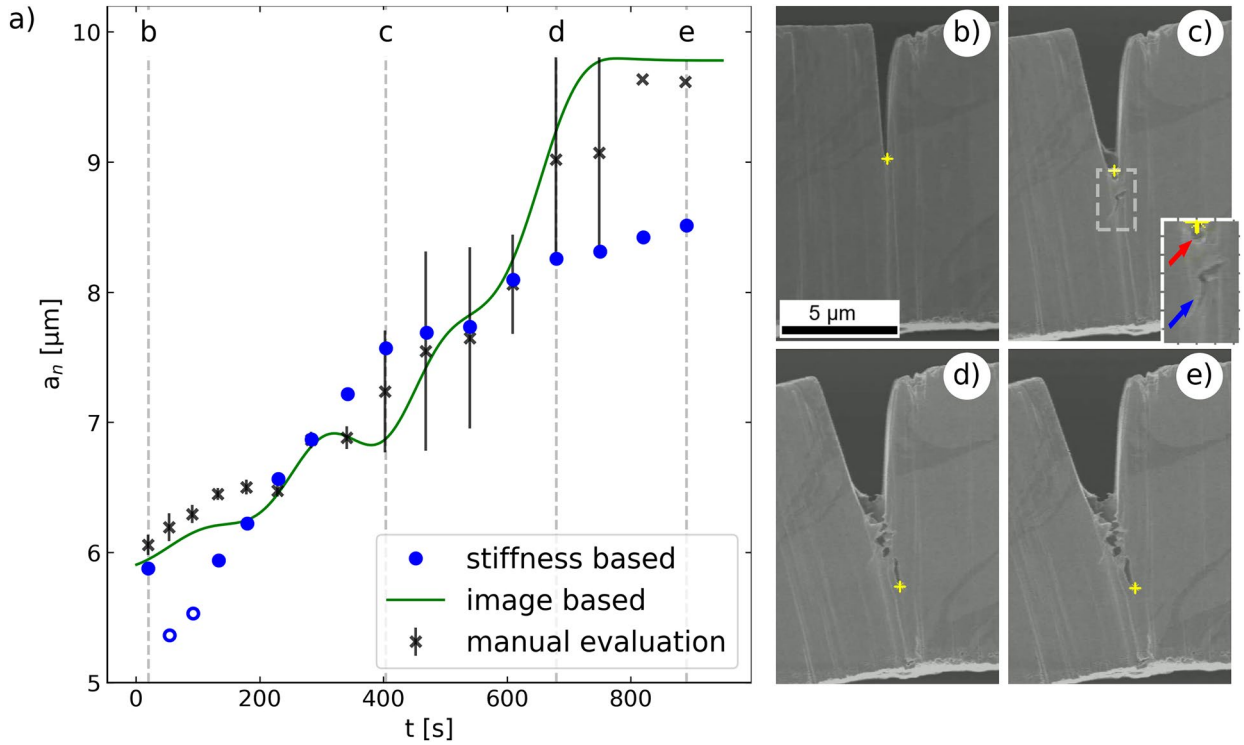

Figure 2: (a) Obtained crack lengths a_n for the medium cantilever with a cross-section of $14.2 \times 13.8\ \mu m^2$. At each unloading step the crack length was measured manually (black crosses) and calculated from unloading stiffness (blue dots), while on each frame the crack length was algorithmically determined (green solid line). Non-physical crack length reduction using stiffness based evaluation are shown by non-filled circles. (b–e) Micrographs of the cracked sample surface at different unloading steps indicated by vertical dashed gray lines in (a). The yellow cross marks the algorithmically identified crack tip. In the inset of (c) the red arrow points to a small crack extension and the blue arrow to pore formation in front of the crack.

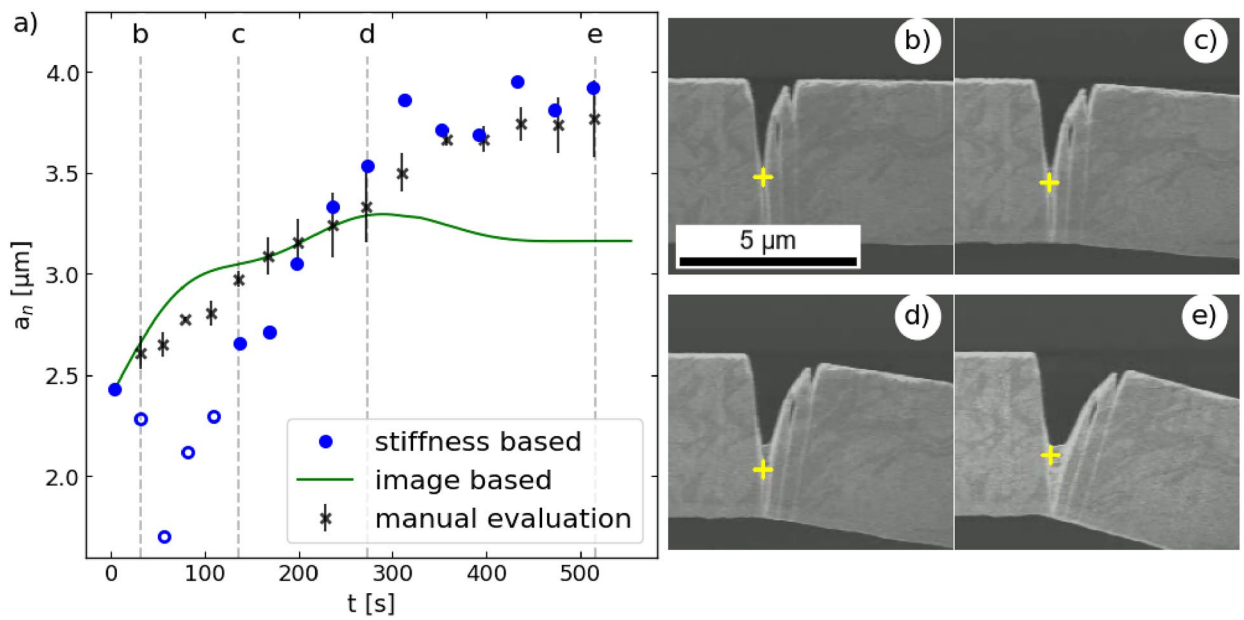

Figure 3: (a) Crack lengths a_n for the smallest cantilever with a cross-section of $6.5 \times 4.3\ \mu m^2$. The algorithm (solid green line) determined crack lengths on each frame, while for each unloading step the crack length was manually measured (black crosses) and calculated from unloading stiffness (blue dots). Non-physical crack lengths of the stiffness based evaluation are marked with non-filled circles. Crack lengths obtained from the algorithm were smoothed by median filtering. Vertical dashed gray lines indicate the unloading steps of (b–e), which the respective micrographs show. The yellow cross marks algorithmically identified crack tips in (b–e).

© The Author(s) 2022

In Fig. 2(a) these two points are shown as non-filled circles. This originates from a stiffness increase for the second and third unloading step compared to the first unloading step. The lower stiffness in the first step might stem from the finite system stiffness and the fact that unloading started directly after loading, resulting in a slight nonlinearity in the unloading segment due to electronic delay. As the initial stiffness used to calculate crack lengths throughout the experiment is found using this first stiffness value, the calculated lengths would be shifted vertically if the changing stiffness were accounted for. Meanwhile, the crack lengths obtained by image-based evaluation methods agree well until position c in Fig. 2(a). At position c a small crack extension was missed by the algorithm, most likely due to contrast variations around the crack tip as depicted with a red arrow in the inset of Fig. 2(c). From position c onwards, the manual measurements started to scatter a lot, because a thin connecting crack to the pore, as depicted by the blue arrow in the inset of Fig. 2(c), was only evident for some measurements. However, from position c to d in Fig. 2(a) only small deviation occurred between manually and algorithmically determined crack length. These deviations stem from elastic closure during unloading due to a closed crack between pore and crack, Figure 2(d). The algorithmically determined crack length between position d and e reached a plateau early, while the manually measured and stiffness calculated crack lengths showed a continuous crack growth until the last unloading step (see Fig. 2(a)). However, at the last unloading position e in Fig. 2(a) the manually and algorithmically evaluated crack lengths agree well, which is also obvious from the corresponding micrograph (see Fig. 2(e)). The crack length calculated from unloading stiffness revealed a shorter crack length of about 1.2 µm compared to the image-based methods. This indicates less crack growth inside the sample. However, 500 nm might be explained by a too low initial stiffness.

For the smallest cantilever ($6.5 \times 4.3\ \mu m^2$), the whole bending beam was imaged, which provides a good overview but also a lower resolution and a lower contrast in the crack vicinity. Nonetheless, Fig. 3(b–e) depict the selected region of interest from the captured images. Due to low contrast, the algorithmic crack length determination required fine-tuning of pre-processing filters to keep the crack separated from surface effects. In addition, manual crack length measurement was challenging due to material bridging and tearing, in addition to the low contrast at the crack tip. Despite these challenges, manually a continuous crack growth was measured at each unloading step. Note that a variation of one pixel amounts to ~ 40 nm, which is equivalent to 1% of the total thickness. Due to the small cantilever cross section only low loads were required for bending, which resulted in a comparatively noisy signal. Therefore, crack evaluation from mechanical data were challenging and the input data were additionally smoothed in a pre-processing step. Crack lengths calculated from unloading stiffness revealed a non-physical crack length reduction between position b and c, marked with non-filled circles in Fig. 3(a). This reduction occurred because the first unloading stiffness is lower than determined stiffness values between position b and c. The reduced stiffness might stem from any of finite system stiffness, a non-linear unloading curve as loading is directly followed by unloading, to low loads especially at the first load cycle, see supplementary. Nevertheless, from a certain point onwards (Fig. 3(c)) crack lengths determined from unloading stiffness showed an overall continuous crack growth. The image-based methods had a roughly constant crack length difference from position b to c (see Fig. 3(a)). There the algorithm detected the crack tip at the bright edge, while manually the crack was located at the end of the dark region (Fig. 3(b, c)). However, between position c and d manual and algorithmic measured crack lengths agree well (see Fig. 3(a)). Further the image-based methods showed a similar crack growth rate of about 2 nm/s from position b to d in Fig. 3(a). However, from position d onwards the algorithm determined a non-physical crack length reduction from 3.3 to 3 µm (see Fig. 3(a)). This is caused by poor resolution, low contrast, contrast changes at the crack tip vicinity and material tearing. The latter started to occur already at position c (see Fig. 3(c)) and increased further until the final unloading (see Fig. 3(d, e)). At the last unloading step the crack length difference between manual measurement and algorithm of about 400 nm is present, depicted in Fig. 3(e).

The J-integral (J) is illustrated over time in Fig. 4 and as classical R-curve against the determined crack extension in Fig. 5, where subfigures (a), (b) and (c) always correspond to the largest, medium and smallest cantilever, respectively. Algorithmically the crack length in each frame during unloading was evaluated, which mathematically allows us to calculate J quasi-continuously, although J is defined for static loading only. Hence, in the present case J is split into loading and unloading including re-loading, which is necessary to reach maximum displacement of the previous loading step. In Figs. 4 and 5, J is depicted with a solid green line for loading and plotted using a grey dashed line during unloading.

J values obtained from algorithmically and manually determined crack lengths agree well for all three specimens (Fig. 4). The evaluated J from the mechanical crack lengths showed slight deviations from $t \approx 500$–850 s and at the two last unloading steps for the largest (see Fig. 4(a)). However, for the medium and smallest specimens, the J values of all three determined crack length sources agree despite the measured crack length scatter, as shown in Fig. 4(b, c). Further, comparing J of all three samples reveals a size effect, which can be seen more clearly in the R-curves by comparing the obtained J values and slopes in Fig. 5(a–c). Moreover, it is obvious to see that the smallest cantilever had a increased J value, which also stems from sample size.

© The Author(s) 2022

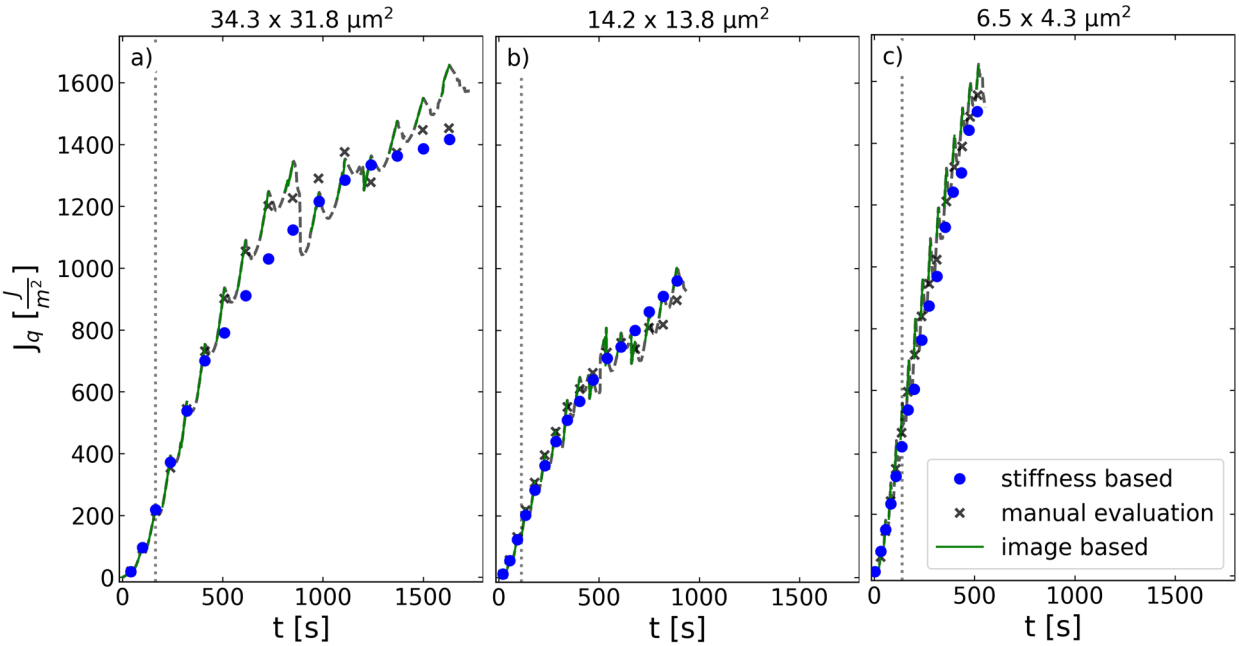

Figure 4: Calculated *J*-integral for the differently determined crack lengths and specimens, where (a) represents the largest, (b) the medium and (c) the smallest cantilever. Blue dots are evaluated from stiffness based evaluations, black crosses rely on manual crack length measurements and the green solid line and the grey dashed line are both determined from algorithmically estimated crack lengths. Note that the gray dashed line represents unloading and re-loading values. Up to the vertical gray dotted line the crack showed crack tip blunting.

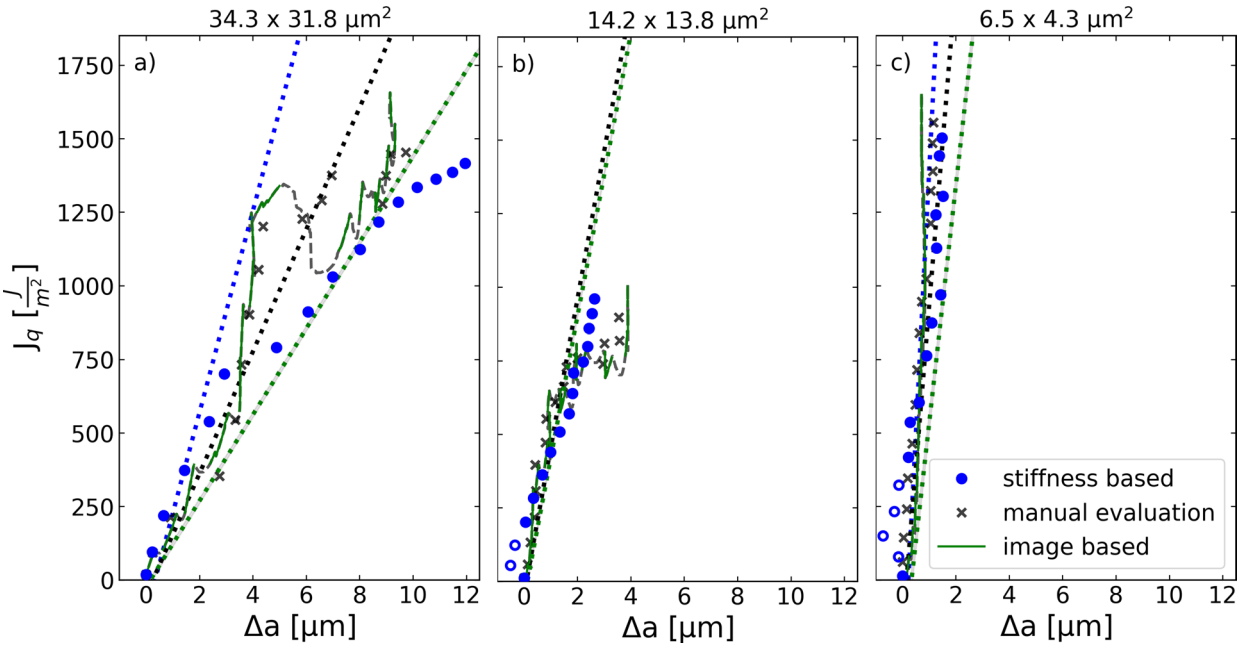

Figure 5: *R*-curve behavior of all three specimens calculated from the differently determined crack lengths, where (a) represents the largest, (b) the medium and (c) the smallest cantilever. Blue dots are evaluated from the stiffness based calculation, black crosses rely on manual crack length measurements, and the green solid line and the grey dashed line are both determined from the algorithmically estimated crack length. Non-physical crack lengths of the stiffness based evaluation are marked with non-filled circles. Note that the gray dashed line represents unloading steps and re-loading. The dotted straight lines represent the fitted shifted blunting lines for each method with the same color code.

© The Author(s) 2022

Further, the standardized evaluation technique for J_{IC} is not applicable, as the sample dimensions are clearly below the crack extension criteria of 200 µm [19]. Thus, the J_q values were determined by following the description in [13], which fits the data in the blunting regime and shifts the fitting line for the half crack tip opening displacement (CTOD). Therefore, for evaluation of J the blunting regime was estimated by manual inspection of the frames, which is hard to visualise. In Fig. 4 the dotted vertical gray line indicates the end of blunting during the experiment. In this region the R-curve values with a positive crack extension were linearly fitted. The CTOD was measured similarly, as described in [21] by inscribing a circle at the crack tip and measuring the diameter, which was done for each specimen on the last frame before evident crack extension occurred. As the frames have a limited resolution the circle was inscribed several times and the mean, as well as the standard deviation, was calculated, resulting in (190 ± 60) nm, (50 ± 10) nm, and (100 ± 40) nm for the large, medium and small-sized cantilevers, respectively. The fitted line in the blunting regime was then shifted by half of the CTOD, as depicted in Fig. 5. The J_q values were determined by intersecting the blunting line with the J-integral points and the closest point was used. In case of no intersection no J_q value was obtained. All determined J_q values are listed in Table 1. The uncertainty of J_{IC} is obtained by shifting the blunting line by the CTOD uncertainty.

For a straightforward comparison with literature and linear elastic fracture mechanics data, the J_{IC} values were converted to K_{IC} values according to ASTM 1820 [19],

$$K_{IC} = \sqrt{\frac{J_{IC}E}{(1-\nu^2)}},$$

with the Young's modulus E = 221 GPa and the Poisons ratio ν = 0.32.

Discussion

All three specimens exhibited a semi-brittle fracture behaviour during bending experiments, as evidenced by pore formation in front of the crack, material bridging and crack bifurcation, as is commonly known for semi-brittle fracture processes [22–25]. Thus, some residual bridges between crack flanks remained, which are desired to increase material toughness, but from the automated crack detection point of view this behaviour gives rise to challenges due to lower local contrast especially at the crack vicinity (see Figs. 1(c–e), 2(c–e) and 3(c–e)). Further, crack detection is complicated by material bridging, tearing and pore formation, as the continuous crack flank might be fragmented into multiple features, refer to Fig. 7(e). For these frames manual evaluation was also challenging and showed low reproducibility due to semi-brittle fracture behavior and the low contrast in the crack tip vicinity. However, image-based crack detection is much simpler for consistently brittle fracture behaviour, such as the fracture of fully lamellar intermetallic TiAl alloys, to which the algorithm was already successfully applied [26].

Besides the already mentioned challenges, the curtain feature introduced by FIB milling below the crack tip affected the ability of the algorithmic results to extract the crack edges and may cause erroneous crack detection. However, fine-tuning of the pre-processing filters was able to alleviate this for all samples. Furthermore, stochastic jumps occurred during algorithmic evaluation between frames due to the aforementioned material bridging and tearing. Thus, median filtering was applied to algorithmically determined crack lengths.

Furthermore, image resolution affects the quality of algorithmic crack flank detections, as the lower resolution limits detection of smaller features. Additionally, it is obvious that reduced sample size decreases feature dimensions, and consequently, detection errors of a few pixels will result in larger crack length deviations. Although the largest cantilever has the lowest image resolution, deviations of a few pixels are negligible compared to the total crack length. For the smallest cantilever a variation of a single pixel (40 nm) represents a change of 1% of the cantilever height.

Despite challenges mentioned above, manual and algorithmic crack length evaluations agree well for the large and medium sized cantilevers, where only slight deviations occur. The image-based evaluation methods did have an increased deviation for a few frames (see Figs. 1(a), 2(a)), but the manual measurement also scattered a lot for these frames, indicating the exact crack tip position was not obvious. Thus, the algorithmically determined crack lengths were within the manual measurement uncertainty (see Figs. 1(a), 2(a)). The image evaluated crack lengths for the smallest cantilever differ over the whole experiment due to low resolution and limited contrast at the crack tip (see Fig. 3(a)).

Evidently, evaluation of each method of this work revealed benefits and drawbacks. Image-based methods capture only the surface part of the three-dimensional crack front. This is an issue as, even for an ideal crack the crack front bends up towards the surface due to the transition from plane strain inside the sample to plane stress on the surface, schematically shown in Fig. 6.

TABLE 1: Evaluated J_q values in J/m^2 for the different methods by intersecting the blunting line with the R-curve. Missing values occurred as the blunting line did not always intersect with the linearly interpolated J-inegral values

Sample/J_q	Stiffness based	Manual	Algorithm
Large	360 ± 50	260 ± 20	–
Medium	–	640 ± 10	590 ± 20
Small	590 ± 30	–	–

© The Author(s) 2022

For isotropic materials Shih [27], established a relation between J-integral and CTOD, which allows a qualitative estimation of the crack length difference between plane strain and plane stress condition by assuming a circular crack tip and relating the CTOD to crack extension

$$\delta = d_n \frac{E}{\sigma_y},$$

with δ_c the CTOD, $d_{n,c}$ the Shih factor for specific Ramberg–Osgood hardening exponent, E the Young's modulus and σ_y, the yield strength. The Young's modulus and yield strength are the same for both conditions, while the CTOD and the Ramberg–Osgood hardening exponent differ. Thus, the CTOD derived from the Shih factor has to be similar for plane strain and plane stress,

$$\frac{\delta_{\text{plane strain}}}{\delta_{\text{plane stress}}} = \frac{d_{\text{plane strain}}}{d_{\text{plane stress}}},$$

The hardening factor of the material was unknown, but the ratio between the Shih factors for different hardening showed almost no variation for this material. Hence, the ratio was approximated by averaging over the Ramberg–Osgood hardening exponents from 2 to 15 [28], revealing a ratio between plane strain and stress of 1.49 ± 0.03. This translates into a longer crack length for the plane strain condition at blunting of 290 nm, 75 nm and 150 nm for the large-, medium- and small-sized cantilevers, respectively. This is negligible compared to the obtained crack lengths. In this model the crack length difference persists between plane strain and stress after blunting and during crack propagation.

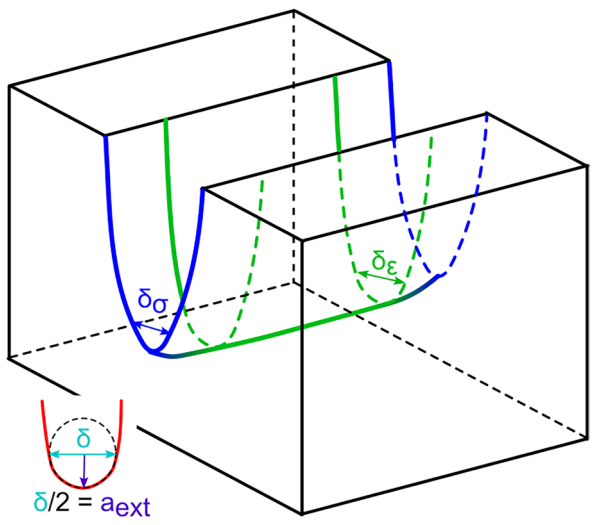

Figure 6: Crack front at blunting, in blue the region where plane stress prevails and in green the plane strain dominated area. A cross-section trough the crack is shown in red in the lower left corner, which depicts an ideal blunted crack with δ as CTOD and a_{ext} as crack extension.

However, in reality, the crack front shape is rather jagged and shows hardly any symmetry [29], due microstructural influences and local strain accumulations. The crack length determined from unloading stiffness gives the average over the whole crack front. Hence, the stiffness-based crack length also captures crack growth inside the sample, but only allows evaluations at discrete unloading steps in this case. Nonetheless, crack growth inside the sample was noticeable for the largest cantilever starting at position c in Fig. 1(a). There the image-based methods missed a possible thin crack, which started to form at position c and steadily grew until the final unloading step. For the medium sized cantilever surface crack growth has started between position c and d in Fig. 2. For this specimen it is also obvious that a well-defined reference stiffness is crucial. Therefore, it is necessary that the load–displacement curve segment during the first unloading segment is straight. This can be achieved by starting unloading from a steady state by adding a hold step between loading and unloading. However, image-based methods measure the crack length bias free from the captured frames. Furthermore manual crack length evaluations are very laborious and user-dependent, while algorithmic crack length determination from images allows evaluation of the crack length of all images in a reasonable time and is less user-dependent, although it still depends on pre-filtering. Evaluation of all available images of a miniaturized in situ experiment provides a higher resolution of individual crack length values compared to the stiffness based approach used. Additionally, the crack lengths of more complicated fracture processes taking place, for example in heterogeneous structures, which have different Young's moduli for each layer, are accessible by image-based methods, while evaluation from mechanical data alone is considerably more challenging due to the necessity of individual simulations. Further, image-based evaluation allows us to determine fracture characteristics during loading, such as crack tip blunting at interfaces, crack branching and deflection [4, 9], which are inaccessible by mechanical data from stiffness based loading.

Based on the differently obtained crack lengths the J values were evaluated for each cantilever. Among one cantilever size the derived J values agree well over time (see Fig. 4). However, among the specimen sizes an increase of the J values is present. This is best seen by comparing the smallest cantilever data (Fig. 4(c)), with the other two in Fig. 4(a, b). The increasing J value can be attributed to a sample size effect, as the plastic zone extends over the whole initial ligament of the smallest cantilever. The R-curve of the largest specimen shows a slope change at larger crack extension, which is best seen in the mechanical data points (Fig. 5(a)). Therefore, the largest cantilever behaves similarly to a macroscopic sample, although it only shows the beginning of the second stage of the R-curve. In the second stage the R-curve starts to flatten and the materials toughness increase is reduced. For the medium sized cantilever, the R-curve has a

© The Author(s) 2022

slightly increased slope and does not show any *R*-curve flattening (see Fig. 5(b)). This can be related to sample size changes, as the *W*/*B* ratio is slightly different to the lager specimen, and the plastic zone takes up a larger fraction of the ligament. However, by comparing the *R*-curve of the large and medium cantilever it is obvious that the *J*-values of the medium-sized cantilever are all within *J* values of the first *R*-curve stage of the largest cantilever, although the *R*-curve slope is increased. In the case of the smallest specimen the *R*-curve slope is strongly increased and shows a continuous increase (Fig. 5(c)). Similar to the increased *J* values this might also provide an indication for a sample size effect, or a crack extension dominated by crack tip blunting.

Evaluation of the J_q values was not possible for all specimens and methods, as the shifted blunting line does not always intersect with the *R*-curve, for example if the blunting line slope is too low (Fig. 5). Further, from mechanical data no blunting line was constructed for the medium sized cantilever, because, by excluding all negative crack extension values, only one value remained, making a linear fit impossible. Nonetheless, determined J_q values agree well within each cantilever size, see Table 1. Evaluated J_q values are sample size independent if the sample dimensions fulfill the condition $B, (W-a) < 10^{J_q}/\sigma_y$. For the validation the yield strength, σ_y was approximated from Vickers hardness measurements with the relationship $\sigma_y \approx 3.3\text{HV}$ [30, 31], which resembles $\sigma_y \approx 1600$ MPa. By assuming the worst case for each specimen using the highest determined J_q, this results in validation values of 2.4 µm, 4 µm and 3.7 µm for the large, medium and small specimens, respectively. Hence, for the larger two specimens the J_q values can be assumed to be sample size independent and are valid J_{IC} values. Conversion of these J_{IC} values gives a K_{IC} value for the largest specimen of 9.5 ± 0.7 MPa $\sqrt{\text{m}}$ and 8 ± 0.4 MPa $\sqrt{\text{m}}$ for mechanical and manual data. The K_{IC} values of the medium-sized cantilever are slightly increased, 12.6 ± 0.2 MPa $\sqrt{\text{m}}$ and 12 ± 1 MPa $\sqrt{\text{m}}$ for manually and algorithmic measured data, respectively. To put these values in context, literature states K_{IC} values of 14 MPa $\sqrt{\text{m}}$ and 9 MPa $\sqrt{\text{m}}$ for polycrystalline textured tungsten at the macro scale with larger grains, for the directions normal to and along the grain texture [32], respectively. The reported K_{IC} values in the current work are in a comparable range, although pure tungsten was used in literature and the grain size is definitely larger compared to the investigated specimens. Magnetron sputtered tungsten, which has a more similar grain size to the investigated samples, shows a fracture toughness ranging from 1 to 2.5 MPa $\sqrt{\text{m}}$ [33]. However, these sputtered films again consist of pure tungsten, while in this work a W-Cu 20%wt was studied. Thus, the fracture toughness deviation can be largely attributed to the different composition, as the ductile copper phase is considered to improve the fracture toughness of tungsten.

Conclusion

In this work a semi-automated technique was proposed to extract the crack length from captured in-situ images at the micron scale. For verification stiffness based bending experiments were performed with differently sized cantilevers, which exhibited semi-brittle fracture behaviour. It was shown that the algorithmically determined crack lengths agree well with manual measurement and crack lengths calculated from unloading stiffness. Where the latter gives discrete values only, the algorithmic image evaluation provides a continuous crack length over the whole experiment, allowing estimation of fracture parameters quasi-continuously. Furthermore, the algorithmic procedure enables investigations of more complicated fracture processes, such as heterogeneous structures, for which mechanical evaluation is not feasible due to, e.g. layer wise variation in Young's moduli or other distributed inhomogeneities. Also materials exhibiting a higher blunting tendency will benefit from this analysis. Taken altogether, this will facilitate more detailed insights into the fracture characteristics of complex high performance materials in future.

Extending the algorithm further to locate and extract both crack flanks as well as the specimen surface edges, it would be possible to obtain additional fracture characteristics, such as crack tip opening displacement, crack tip-opening angle and crack mouth opening displacement.

Methodology and experimental

Experimental

The samples investigated in this study were fabricated from a rod with a diameter of 8 mm and the material composition W-Cu 20%wt. From this material, disks were cut with a thickness of 0.8 mm and subjected to high pressure torsion (HPT) up to an equivalent strain of 120. This resulted in a bi-modal microstructure with a nano-crystalline matrix with a mean grain size of about 10 ± 4 nm and some statistically distributed elongated *W* inhomogeneities. Corresponding micrographs are shown in the supplementary. Further, the HPT process reduced the sample thickness to about 0.5 mm. The HPT disks were cut into halves, which were manually ground and polished down to a thickness of approximately 50 µm to reduce FIB time.

Three differently sized cantilever beams were fabricated by combined femtosecond laser ablation [34] for coarse machining, and FIB milling for fine cutting, within a scanning electron microscope (SEM/FIB; Zeiss Auriga Laser platform, Carl Zeiss AG, Oberkochen, Germany). The FIB current was subsequently decreased from 10 nA for coarse milling to 500 pA for the final polishing step. The fabricated cantilever had cross-sections ($W \times B$) of 34.3×31.8 µm^2, 14.2×13.8 µm^2 and 6.5×4.3 µm^2 as well as lengths of 150.6 µm, 82.9 µm, and 35.8 µm, respectively.

© The Author(s) 2022

For each cantilever, a notch was introduced in top-view by line milling with a current of 500 pA to depths of about $0.4 \times W$. The notch of the largest cantilever required a precutting from the side-view to reach the required depth and was afterward finalized in top-view as well.

Mechanical tests were performed with a micro indenter (UNAT_SEM 1, ASMEC GmbH, Dresden, Germany) which operates in a displacement controlled open-loop mode. In vacuum, the indenter has an undamped force noise level of 50 µN. and was situated inside a scanning electron microscope (DSM 982, Carl Zeiss AG, Oberkochen, Germany) to record in-situ images at a rate of one image per second during the experiments. For the experiments, a constant displacement rate of 0.05 µm/s was used. Furthermore, for each cantilever 15 unloading steps were performed, which consisted of a displacement drop of at least 10% of the current displacement, but at maximum 2 µm. For the largest, medium, and smallest cantilevers the maximum displacement was set to 32 µm, 16 µm, and 8 µm, respectively. One loading cycle consists of loading, unloading and a hold segment of about 10 s before the next loading cycle starts. For the smallest cantilever, the entire bending beam was imaged, while for the two larger cantilevers, the image area was limited to the crack tip vicinity. Images were captured using an in-lens secondary electron detector for all three samples.

Image-based crack length measurement

The image acquisition rate defines the time resolution during small-scale in-situ fracture experiments. Typically, these experiments are performed within an SEM, where image quality suffers due to high image acquisition rates necessary to monitor crack growth.

Digital image analysis aims to extract information from an image by utilizing feature extraction, optical flow, image segmentation, or edge detection methods [14, 35–38]. The former two did not apply to in-situ crack growth images captured by SEM, as the recorded images contain only a limited amount of properly recognisable features on each individual frame. Image segmentation simplifies an image by partitioning it into segments, e.g. background-sample, and does not rely on proper feature detection between frames. However, due to the low contrast in the crack tip vicinity, application of image segmentation is difficult. On the other hand, edge detection extracts edges from the image by calculating the image gradient and thresholds the image gradient for edge extraction. This allows detection of edges on each frame and localize the crack flank.

Pre-processing

The proposed algorithm was implemented in Python 3.8 [39] utilizing Numpy 1.20.2 [40], Scipy 1.5.4 [41], and Scikit-Learn 0.24.1 [42]. Image processing was done via the python-based OpenCv community library 4.5.1.18 [43] as well as Scikit-Image 0.18.0 [44]. Captured images are typically noisy due to the high image acquisition rates when monitoring crack growth due to non-uniform illumination [14, 45]. Hence, a few pre-processing steps were required: First a region of interest (ROI) was selected to reduce the computational burden (Fig. 7(a)). For this selection, it had to be ensured that the crack was within this ROI on all frames.

Noise was reduced by filtering, involving Non-local Means filter (NLM) [46] and, if necessary, Gaussian blurring. The former does a decent job of reducing speckle as well as salt and pepper noise, which is randomly distributed bright and dark pixels due to detector disturbance. NLM filtering consists of the parameters: filter strength, which is directly related to noise removal, patch sizes, used to calculate weights, and search window size, defining the regions considered to compute the average pixel value (see Fig. 7(b)). However, to prevent NLM from edge blurring, the filter strength value has to be used in moderation. In this work, suitable values were found in the range from 0 to 10. Gaussian blur does significantly reduce white noise, but at the cost of a blurred image, shown in Fig. 7(c). For that, the Gaussian blur computes a normalized weighted average value to set the central pixel of the considered region. The filter process is adjusted by the kernel size, defining the considered region and standard deviation, from which weights are computed.

To enhance contrast and improve segmentation between sample and background, contrast limited adaptive histogram equalization (CLAHE) [47] was applied, which enhances bright and dark regions equally, as seen in Fig. 7(d). This is done after noise removal to avoid undesired noise enhancement. As filter parameters, CLAHE takes the number of tiles used to split the image into equal spaced sub-regions and clip limit, defining the limiting count for each bin of the histogram. For each sub-region, the algorithm calculates a histogram and equally redistributes all values above the clip limit, which should be in the range from 1 to 5 to ensure reasonable results and to avoid noise enhancement due to maximizing local contrast.

Image segmentation is realized using the Canny method [35], which is a well-established technique to extract edges from images. The Canny parameters are kernel size, defining the considered region for gradient calculation and two thresholds, which are used to locate edges on the intensity gradient image. Gradient values above both thresholds are considered as strong edges, while gradient values between them are weak edges and only contribute to an edge if they are connected to a strong edge. All gradients below both thresholds are rejected, leading to a binary segmented image. Finally, to extract the edge location, border following was applied [48].

© The Author(s) 2022

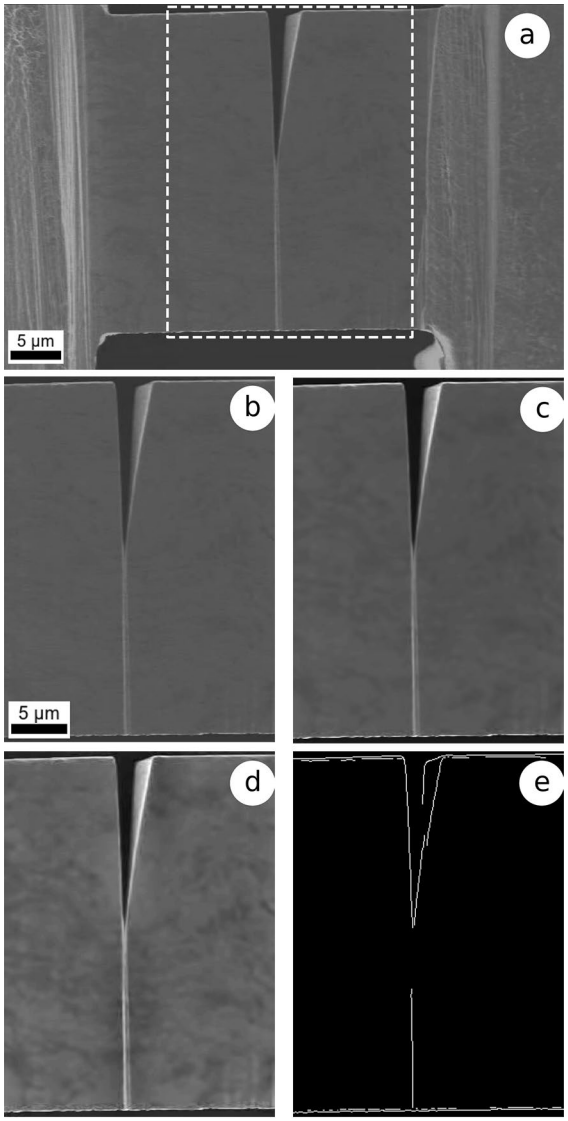

Figure 7: Subsequent pre-processing steps for crack length determination. (a) Original SEM image with a dashed white rectangle for ROI selection, (b) NLM filtering, (c) Gaussian blur, (d) Enhance contrast with CLAHE, (e) Edge extraction with Canny algorithm.

Crack length measurement

According to ASTM E399 [49] crack length is the average crack front extension into the sample. However, images captured via SEM represent only the surface projection of the crack flank. Hence, for images, the crack length is taken as the furthest crack extension into the sample material on the surface.

To measure crack lengths from images it was necessary to locate the crack tip on each frame from the extracted edges. Therefore, only minor position changes of the crack flank were assumed between consecutive frames near the crack tip (< 25 pixels). This allows a crack flank to be obtained on the following frame by calculating the pair wise distance between the current crack flank

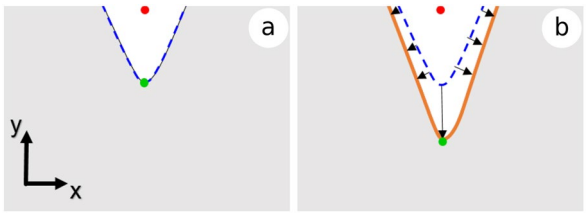

Figure 8: Schematic crack flank detection on consecutive frames: (a) Previous frame with the located crack flank (dashed blue line). (b) Following frame with the previously found crack flank (dashed blue line), a possible found contour line (orange solid line), representative distance measure between previous crack flank and contour line for all pixels on that contour line (black arrows), reference point for measurement (red dot) and the possible crack tip (green dot).

pixels and all pixels of each new extracted edge. For each contour line the minimal distance between each pixel and the current crack flank was calculated. These distances were then summed and divided by the length of the edge and current crack flank for normalization. This should ensure preference for longer edges over small ones. The edge with the smallest resulting value from this procedure is selected as the new crack flank. From these newly selected crack flanks, the crack tip is determined by assuming that the crack tip lies on the newly selected crack flank and that it is the point that extends furtherst into the material (see Fig. 8). Thus, the point on the newly selected crack flank which is maximised in crack growth direction is selected as new crack tip.

However, this procedure does not reliably detect the whole crack flank, because extracted edges are often detached from each other and may represent only a fragment of the crack flank. Multiple edges are combined to form a new crack flank. Hence, the crack length was calculated as the distance between a fixed point on the top surface of the cantilever and the determined crack tip. Further, algorithmically obtained crack lengths were median filtered to remove outliners, which might occur due to fragmented crack flanks as well as low contrast and resolution around the crack tip.

Crack length estimation from mechanical data

Mechanical data was used to estimate the average crack length over the cantilever cross-section. For that the recorded load and displacement data were smoothed by low pass filtering in a forward and backward manner [50] to reduce noise. Following the description in [20] crack lengths were calculated by relating stiffness changes to cross-section reduction at expense of crack growth. Stiffness changes were calculated by linear regression from the load–displacement curve during unloading as described in [15]. From the first unloading stiffness and the corresponding crack length, the initial stiffness was calculated, which was used as reference.

© The Author(s) 2022

J-integral evaluation

Mechanical data and sample dimensions were used in conjunction with the differently obtained crack lengths to calculate the J for each specimen according to elastic plastic fracture mechanics by following the iterative procedure described in ASTM 1820 [19],

$$J(a) = J^{\mathrm{el}}(a) + J^{\mathrm{pl}}(a),$$

$$J_n^{\mathrm{el}} = \frac{K_{q,n}^2(1-\nu^2)}{E},$$

$$J_n^{\mathrm{pl}} = \left(J_{n-1}^{\mathrm{pl}} + \frac{\eta_{n-1}^{\mathrm{pl}}}{W-a_{n-1}}\frac{A_n^{\mathrm{pl}} - A_{n-1}^{\mathrm{pl}}}{B}\right)\left(1-\gamma\frac{a_n - a_{n-1}}{W-a_{n-1}}\right),$$

with the iteration step number n, the elastic part J^{el} and the plastic part J^{pl} of the J-integral at a specific crack length a_n. Geometry independent pre-factors $\eta = 1.9$ and $\gamma = 0.9$ were used as stated by ASTM 1820 [19] for single edge notched bend specimen due to the loading similarities between this geometry and cantilever shaped beams. The Young's modulus was set to $E = 221$ GPa and the Poissons ratio was substituted with $\nu = 0.32$. The stress intensity factor K_q was calculated according to ASTM 399 [49],

$$K_n = \frac{F_n L}{B W^{\frac{3}{2}}} f\left(\frac{a_n}{W}\right),$$

with the load given as F and the geometry factor as $f(\frac{a}{W})$, where the function proposed by Riedl et al. [5] was used. The geometry dependent variables B, W and L were sample width, -thickness and length, respectively, as seen in Fig. 9. Further from the load–displacement curve the plastic work at each step is calculated according to [21],

$$A_n^{\mathrm{pl}} = A_n^{\mathrm{tot}} - A_n^{\mathrm{el}} = \int_0^{u_n} F\mathrm{d}u - \frac{F_n^2}{2k_n},$$

where u_n is the mechanical displacement, F_n the load at unloading and k_n the corresponding stiffness. Note that for the image-based evaluation methods the stiffness was estimated from the crack length by numerical evaluation of

$$k_n = k_0 \frac{1}{\left(1+18\left(1-\nu^2\right)\right)\frac{L^2}{L'^3}\int_0^a \frac{a}{W} f\left(\frac{a}{W}\right)^2},$$

with k_0 as initial stiffness from the first unloading step and L as length between crack and loading point.

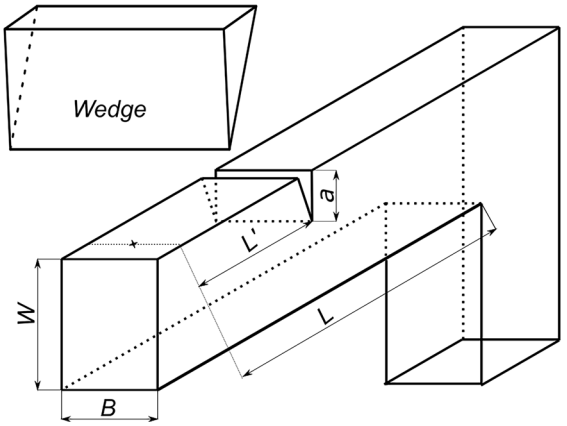

Figure 9: Cantilever geometry with thickness W, width B, notch depth a, length to the notch L, and the length to the base L'.

Acknowledgments

The authors thank Dr. Michael Burtscher for the TEM analysis.

Author contributions

Conceptualization, DK and KS; methodology, MA and KS; software, KS; validation, KS; formal analysis, KS and MA; investigation, MA and KS; resources, DK; data curation, KS; writing—original draft preparation, KS; writing—review and editing, KS, MA and DK; supervision, DK; project administration, DK; funding acquisition, DK. All authors have read and agreed to the published version of the manuscript.

Funding

The authors acknowledge funding provided by the European Research Council under Grant Number: 771146 (TOUGHIT).

Data availability

The data sets generated during the current study are available from the corresponding author on a reasonable request.

Code availability

The data sets generated during the current study are available from the corresponding author on a reasonable request.

Declarations

Conflict of interest The authors declare that they have no known competing financial interests or personal relationships that could have appeared to influence the work reported in this paper.

Supplementary Information

The online version contains supplementary material available at https://doi.org/10.1557/s43578-022-00681-4.

© The Author(s) 2022

Open Access

This article is licensed under a Creative Commons Attribution 4.0 International License, which permits use, sharing, adaptation, distribution and reproduction in any medium or format, as long as you give appropriate credit to the original author(s) and the source, provide a link to the Creative Commons licence, and indicate if changes were made. The images or other third party material in this article are included in the article's Creative Commons licence, unless indicated otherwise in a credit line to the material. If material is not included in the article's Creative Commons licence and your intended use is not permitted by statutory regulation or exceeds the permitted use, you will need to obtain permission directly from the copyright holder. To view a copy of this licence, visit http://creativecommons.org/licenses/by/4.0/.

References

1. K.S. Ng, A.H.W. Ngan, Effects of trapping dislocations within small crystals on their deformation behavior. Acta Mater. **57**, 4902–4910 (2009). https://doi.org/10.1016/j.actamat.2009.06.053
2. J.A. El-Awady, S.I. Rao, C. Woodward, D.M. Dimiduk, M.D. Uchic, Trapping and escape of dislocations in micro-crystals with external and internal barriers. Int. J. Plast. **27**, 372–387 (2011). https://doi.org/10.1016/j.ijplas.2010.06.006
3. J.R. Greer, J.T.M. De Hosson, Plasticity in small-sized metallic systems: intrinsic versus extrinsic size effect. Prog. Mater. Sci. **56**, 654–724 (2011). https://doi.org/10.1016/j.pmatsci.2011.01.005
4. R. Treml, D. Kozic, R. Schöngrundner, O. Kolednik, H.P. Gänser, R. Brunner, D. Kiener, Miniaturized fracture experiments to determine the toughness of individual films in a multilayer system. Extrem. Mech. Lett. **8**, 235–244 (2016). https://doi.org/10.1016/j.eml.2016.01.004
5. A. Riedl, R. Daniel, M. Stefenelli, T. Schöberl, O. Kolednik, C. Mitterer, J. Keckes, A novel approach for determining fracture toughness of hard coatings on the micrometer scale. Scr. Mater. **67**, 708–711 (2012). https://doi.org/10.1016/j.scriptamat.2012.06.034
6. D.E.J. Armstrong, M.E. Rogers, S.G. Roberts, Micromechanical testing of stress corrosion cracking of individual grain boundaries. Scr. Mater. **61**, 741–743 (2009). https://doi.org/10.1016/j.scriptamat.2009.06.017
7. K. Matoy, T. Detzel, M. Müller, C. Motz, G. Dehm, Interface fracture properties of thin films studied by using the micro-cantilever deflection technique. Surf. Coat. Technol. **204**, 878–881 (2009). https://doi.org/10.1016/j.surfcoat.2009.09.013
8. D.S. Gianola, A. Sedlmayr, R. Mnig, C.A. Volkert, R.C. Major, E. Cyrankowski, S.A.S. Asif, O.L. Warren, O. Kraft, In situ nanomechanical testing in focused ion beam and scanning electron microscopes. Rev. Sci. Instrum. **82**, 1–12 (2011). https://doi.org/10.1063/1.3595423
9. J. Ast, M. Ghidelli, K. Durst, M. Göken, M. Sebastiani, A.M. Korsunsky, A review of experimental approaches to fracture toughness evaluation at the micro-scale. Mater. Des. **173**, 107762 (2019). https://doi.org/10.1016/j.matdes.2019.107762
10. P. Hosemann, Small-scale mechanical testing on nuclear materials: bridging the experimental length-scale gap. Scr. Mater. **143**, 161–168 (2018). https://doi.org/10.1016/j.scriptamat.2017.04.026
11. G. Dehm, B.N. Jaya, R. Raghavan, C. Kirchlechner, Overview on micro- and nanomechanical testing: new insights in interface plasticity and fracture at small length scales. Acta Mater. **142**, 248–282 (2018). https://doi.org/10.1016/j.actamat.2017.06.019
12. J.C. Lindsay, in *In Situ Measurement of Fatigue Induced Crack Growth in Inconel 718 Using Direct Current Potential Drop Method*. Statler College of Engineering and Mineral Resources (2019). https://doi.org/10.33915/etd.4050
13. C. Bohnert, N.J. Schmitt, S.M. Weygand, O. Kraft, R. Schwaiger, Fracture toughness characterization of single-crystalline tungsten using notched micro-cantilever specimens. Int. J. Plast. **81**, 1–17 (2016). https://doi.org/10.1016/j.ijplas.2016.01.014
14. M. Sutton, J.-J. Orteu, H. Schreier, *Image Correlation for Shape, Motion and Deformation Measurements* (Springer, Berlin, Heidelberg, 2009). https://doi.org/10.1007/978-0-387-78747-3
15. S. Wurster, C. Motz, R. Pippan, Characterization of the fracture toughness of micro-sized tungsten single crystal notched specimens. Philos. Mag. **92**, 1803–1825 (2012). https://doi.org/10.1080/14786435.2012.658449
16. J. Ast, B. Merle, K. Durst, M. Göken, Fracture toughness evaluation of NiAl single crystals by microcantilevers—a new continuous J-integral method. J. Mater. Res. **31**, 3786–3794 (2016). https://doi.org/10.1557/jmr.2016.393
17. F. Iqbal, J. Ast, M. Göken, K. Durst, In situ micro-cantilever tests to study fracture properties of NiAl single crystals. Acta Mater. **60**, 1193–1200 (2012). https://doi.org/10.1016/j.actamat.2011.10.060
18. J. Ast, T. Przybilla, V. Maier, K. Durst, M. Göken, Microcantilever bending experiments in NiAl—evaluation, size effects, and crack tip plasticity. J. Mater. Res. **29**, 2129–2140 (2014). https://doi.org/10.1557/jmr.2014.240
19. ASTM Standard E1820, Standard Test Method for Measurement of Fracture Toughness, ASTM B. Stand. (2013), pp. 1–54. https://doi.org/10.1520/E1820-13.Copyright
20. M. Alfreider, S. Kolitsch, S. Wurster, D. Kiener, An analytical solution for the correct determination of crack lengths via cantilever stiffness. Mater. Des. **194**, 3–7 (2020). https://doi.org/10.1016/j.matdes.2020.108914
21. M. Alfreider, D. Kozic, O. Kolednik, D. Kiener, In-situ elastic-plastic fracture mechanics on the microscale by means of continuous dynamical testing. Mater. Des. **148**, 177–187 (2018). https://doi.org/10.1016/j.matdes.2018.03.051

© The Author(s) 2022

22. R.M.N. Pelloux, Crack extension by alternating shear. Eng. Fract. Mech. **1**, 697–700 (1970). https://doi.org/10.1016/0013-7944(70)90008-1
23. R.O. Ritchie, Mechanism of fatigue-crack propagation in ductile and brittle materials. Int. J. Fract. **100**, 55–83 (1998)
24. J.E. Hack, S.P. Chen, D.J. Srolovitz, A kinetic criterion for quasi-brittle fracture. Acta Metall. **37**, 1957–1970 (1989). https://doi.org/10.1016/0001-6160(89)90080-1
25. R. Pippan, S. Wurster, D. Kiener, Fracture mechanics of micro samples: fundamental considerations. Mater. Des. **159**, 252–267 (2018). https://doi.org/10.1016/j.matdes.2018.09.004
26. M. Burtscher, M. Alfreider, K. Schmuck, H. Clemens, S. Mayer, D. Kiener, In situ fracture observations of distinct interface types within a fully lamellar intermetallic TiAl alloy. J. Mater. Res. **36**, 2465–2478 (2021). https://doi.org/10.1557/jmr.2020.306
27. C.F. Shih, Relationship between the J-integral and the COD for stationary and extending cracks. J. Mech. Phys. Solids **29**, 305–326 (1981)
28. W. Brocks, D. Klingbeil, J. Olschewski, Lösung der HRR-Feld-Gleichungen der elastisch-plastischen Bruchmechanik, Bremerhaven (1990)
29. A.K. Saxena, S. Brinckmann, B. Völker, G. Dehm, C. Kirchlechner, Experimental conditions affecting the measured fracture toughness at the microscale: notch geometry and crack extension measurement. Mater. Des. **191**, 1–11 (2020). https://doi.org/10.1016/j.matdes.2020.108582
30. P.G. Sanders, C.J. Youngdahl, J.R. Weertman, The strength of nanocrystalline metals with and without flaws. Mater. Sci. Eng. A. **234–236**, 77–82 (1997). https://doi.org/10.1016/s0921-5093(97)00185-8
31. P. Zhang, S.X. Li, Z.F. Zhang, General relationship between strength and hardness. Mater. Sci. Eng. A **529**, 62–73 (2011). https://doi.org/10.1016/j.msea.2011.08.061
32. D. Rupp, S.M. Weygand, Experimental investigation of the fracture toughness of polycrystalline tungsten in the brittle and semi-brittle regime. J. Nucl. Mater. **386–388**, 591–593 (2009). https://doi.org/10.1016/j.jnucmat.2008.12.184
33. E. Harry, A. Rouzaud, P. Juliet, Y. Pauleau, M. Ignat, Failure and adhesion characterization of tungsten-carbon single layers, multilayered and graded coatings. Surf. Coat. Technol. **116–119**, 172–175 (1999). https://doi.org/10.1016/S0257-8972(99)00071-7
34. M.J. Pfeifenberger, M. Mangang, S. Wurster, J. Reiser, A. Hohenwarter, W. Pfleging, D. Kiener, R. Pippan, The use of femtosecond laser ablation as a novel tool for rapid micro-mechanical sample preparation. Mater. Des. **121**, 109–118 (2017). https://doi.org/10.1016/j.matdes.2017.02.012
35. J. Canny, A computational approach to edge detection. IEEE Trans. Pattern Anal. Mach. Intell. **PAMI-8**, 679–698 (1986). https://doi.org/10.1109/TPAMI.1986.4767851
36. D. Vikram Mutneja, Methods of image edge detection: a review. J. Electr. Electron. Syst. **4**, 1–5 (2015). https://doi.org/10.4172/2332-0796.1000150
37. M. Vidal, M. Ostra, N. Imaz, E. García-Lecina, C. Ubide, Analysis of SEM digital images to quantify crack network pattern area in chromium electrodeposits. Surf. Coat. Technol. **285**, 289–297 (2016). https://doi.org/10.1016/j.surfcoat.2015.11.049
38. C. Roux-Langlois, A. Gravouil, M.C. Baietto, J. Réthoré, F. Mathieu, F. Hild, S. Roux, DIC identification and X-FEM simulation of fatigue crack growth based on the Williams' series. Int. J. Solids Struct. **53**, 38–47 (2015). https://doi.org/10.1016/j.ijsolstr.2014.10.026
39. G. Van Rossum, F.L. Drake, *Python 3 Reference Manual*. (CreateSpace, Scotts Valley, 2009). https://www.python.org/. Accessed 9 Aug 2021
40. C.R. Harris, K.J. Millman, S.J. van der Walt, R. Gommers, P. Virtanen, D. Cournapeau, E. Wieser, J. Taylor, S. Berg, N.J. Smith, R. Kern, M. Picus, S. Hoyer, M.H. van Kerkwijk, M. Brett, A. Haldane, J. Fernández del Río, M. Wiebe, P. Peterson, P. Gérard-Marchant, K. Sheppard, T. Reddy, W. Weckesser, H. Abbasi, C. Gohlke, T.E. Oliphant, Array programming with {NumPy}. Nature **585**, 357–362 (2020). https://doi.org/10.1038/s41586-020-2649-2
41. P. Virtanen, R. Gommers, T.E. Oliphant, M. Haberland, T. Reddy, D. Cournapeau, E. Burovski, P. Peterson, W. Weckesser, J. Bright, S.J. van der Walt, M. Brett, J. Wilson, K.J. Millman, N. Mayorov, A.R.J. Nelson, E. Jones, R. Kern, E. Larson, C.J. Carey, I. Polat, Y. Feng, E.W. Moore, J. VanderPlas, D. Laxalde, J. Perktold, R. Cimrman, I. Henriksen, E.A. Quintero, C.R. Harris, A.M. Archibald, A.H. Ribeiro, F. Pedregosa, P. van Mulbregt, SciPy 1.0: fundamental algorithms for scientific computing in Python. Nat. Methods **17**, 261–272 (2020). https://doi.org/10.1038/s41592-019-0686-2
42. F. Pedregosa, G. Varoquaux, A. Gramfort, V. Michel, B. Thirion, O. Grisel, M. Blondel, P. Prettenhofer, R. Weiss, V. Dubourg, J. Vanderplas, A. Passos, M. Cournapeau, D. Brucher, M. Perrot, É. Duchesnay, Scikit-learn: machine learning in Python. J. Mach. Learn. Res. **12**, 2825–2830 (2011)
43. G. Bradski, The OpenCV Library, Dr. Dobb's J. Softw. Tools. (2000). https://docs.opencv.org/4.3.0/. Accessed 9 Aug 2021
44. S. van der Walt, J.L. Schönberger, J. Nunez-Iglesias, F. Boulogne, J.D. Warner, N. Yager, E. Gouillart, T. Yu, Scikit-image: image processing in Python. PeerJ (2014). https://doi.org/10.7717/peerj.453
45. A.D. Kammers, S. Daly, Digital image correlation under scanning electron microscopy: methodology and validation. Exp. Mech. **53**, 1743–1761 (2013). https://doi.org/10.1007/s11340-013-9782-x
46. A. Buades, B. Coll, J.-M. Morel, Non-local means denoising. Image Process. Line **1**, 208–212 (2011). https://doi.org/10.5201/ipol.2011.bcm_nlm

© The Author(s) 2022

47. S.M. Pizer, E.P. Amburn, J.D. Austin, R. Cromartie, A. Geselowitz, T. Greer, B. ter Haar Romeny, J.B. Zimmerman, K. Zuiderveld, Adaptive histogram equalization and its variations. Comput. Vis. Graph. Image Process. **39**, 355–368 (1987). https://doi.org/10.1016/S0734-189X(87)80186-X
48. S. Suzuki, K. Abe, Topological structural analysis of digitized binary images by border following. Comput. Vis. Graph. Image Process. **30**, 32–46 (1985). https://doi.org/10.1016/0734-189X(85)90016-7
49. ASTM Standard E399-90, *Standard Test Method for Linear-Elastic Plane-Strain Fracture Toughness KIC of Metallic Materials* (1997), pp. 413–433. https://doi.org/10.1520/E0399-90R97
50. F. Gustafsson, Determining the initial states in forward-backward filtering. IEEE Trans. Signal Process. **44**, 988–992 (1996). https://doi.org/10.1109/78.492552

© The Author(s) 2022